Nanoscale

PAPER

View Article Online
View Journal

Cite this: DOI: 10.1039/d5nr05237h

Rational design of Pickering emulsion-templated silica capsules loaded with ionic liquids: tailoring intrinsic textural properties *via* interfacial sol–gel kinetics

Rémi Duclos,*[a,c] Dina Lofficial,[a] David Proriol,[a] Christine Dalmazzone,[b] Stéphane Parola[c] and Frédéric Lerouge[c]

The encapsulation of ionic liquids (ILs) within porous silica capsules templated from a Pickering emulsion offers a powerful platform for designing efficient microreactors in biphasic systems. However, a fundamental understanding of how synthesis parameters govern the textural properties and structural integrity of the porous silica capsules remains limited. This study presents a comprehensive investigation into the sol–gel synthesis of IL-containing silica capsules, establishing crucial structure–property relationships. We demonstrate that for the study of textural properties, supercritical CO_2 drying is a prerequisite for preserving the capsule's native morphology and porosity, whereas conventional ambient drying causes severe shrinkage and structural collapse due to capillary forces. Leveraging this preservation method, we show that acidic catalysis (more precisely, at pH below the isoelectric point of silica, which is pH < 2) favors the formation of highly mesoporous capsules with better structural cohesion, while basic conditions result in capsules more prone to severe fragmentation. Furthermore, optimization of the reaction temperature, time and water-to-alkoxysilane ratio is found to be essential for balancing shell growth kinetics with mechanical stability. These findings provide a rational framework for engineering robust, tailored silica capsules for advanced applications in catalysis and controlled release.

Received 12th December 2025,
Accepted 19th May 2026

DOI: 10.1039/d5nr05237h

rsc.li/nanoscale

1. Introduction

Encapsulation technology has emerged as a crucial strategy in materials science and chemistry, enabling the controlled containment and targeted release of active compounds for diverse applications spanning drug delivery, self-healing materials, and energy storage.[1–4] Among the various encapsulation approaches, silica-based capsules have attracted considerable attention due to their exceptional chemical stability, biocompatibility, tunable porosity, and versatile surface chemistry.[5] These properties render silica capsules particularly promising for applications requiring precise control over the loading, protection, and release of encapsulated substances.[1] Beyond these established applications in containment and delivery, silica-based capsules can also be used in biphasic systems, where they function as efficient microreactors. In this configuration, the porous shell increases the effective interfacial contact area between the confined catalytic phase and the surrounding medium, enhances catalyst recyclability, and imparts resistance to pressure, shear, and concentration fluctuations that would typically destabilize conventional emulsions while permitting free diffusion of substrates and products, effectively bridging the gap between homogeneous and heterogeneous catalysis.[6,7] This encapsulation strategy could be particularly valuable for stabilizing sensitive catalytic systems that are industrially relevant such as various hydrogenation and dimerization reactions or olefin hydroformylation.[8–10] Crucially, these reactions often employ ionic liquids as the sequestered solvent phase, leveraging their unique physicochemical properties to solubilize transition metal complexes while remaining securely trapped within the silica shell.[9,11–13]

Ionic liquids (ILs) are organic salts with melting points below 100 °C, representing a mature and rapidly growing class of multifunctional materials with diverse applications spanning chemistry, energy, biomedicine, and environmental remediation.[14–16] Their unique physicochemical properties—including low volatility, high thermal and chemical stability, non-flammability, wide electrochemical windows, and tunable design—make them superior alternatives to traditional

[a]IFP Energies Nouvelles – Etablissement de Lyon, Rond-point de l'échangeur de Solaize, 69360 Solaize, France. E-mail: dina.lofficial@ifpen.fr
[b]IFP Energies Nouvelles, 1 et 4 avenue de Bois-Préau, 92852 Rueil-Malmaison Cedex, France
[c]Laboratoire de Chimie de l'ENS de Lyon, 46 allée d'Italie, 69364 Lyon Cedex 07, France. E-mail: frederic.lerouge@ens-lyon.fr

organic solvents.[14–16] When confined in porous materials, ILs exhibit significantly enhanced performance through increased surface contact areas and altered physicochemical properties.[7,17–19] Encapsulated ILs demonstrate dramatically improved CO_2 absorption rates while maintaining high capacity, enhanced mass transfer for gas separation, controlled drug delivery with improved solubility and bioavailability, and superior catalytic activity in heterogeneous systems.[7,17–19]

Pickering emulsions—emulsions stabilized by solid particles adsorbed at liquid–liquid interfaces rather than by molecular surfactants—are widely used as templates for synthesizing silica capsules with well-defined morphologies. The use of Pickering emulsions offers several advantages over conventional emulsion-based approaches. First, the irreversible adsorption of particles at the interface provides exceptional long-term stability to the emulsion droplets.[20] Second, the absence of molecular surfactants eliminates concerns about surfactant removal and potential contamination of the final product.[20] Third, the particles themselves can participate in or direct the shell formation process, leading to unique composite structures.[21] Pickering emulsions are then used as templates to form hollow silica capsules thanks to an interfacial sol–gel polycondensation process that occurs at the interface between the dispersed and continuous phases, where alkoxysilane precursors react with water to form a silica shell encapsulating the core material.[22–24]

Controlling the textural properties of the formed capsules is very important depending on their application. The modification of the textural properties of porous silica is a very well documented subject in the literature. The best-known method is surfactant templating, which provides precise mesopore control by forming micelle assemblies that direct pore architecture.[25–27] The surfactant chain length and concentration enable systematic pore size tuning.[26,27] Mixed surfactant systems introduce bimodal or hierarchical porosity by combining templates with different molecular sizes.[28] This addition of surfactant is always followed by calcination in order to eliminate the surfactant and create porosity in the material. However, surfactant templating is fundamentally incompatible with Pickering emulsion templated silica capsules for introducing porosity in silica capsules due to competing and contradictory stabilization mechanisms that operate at the emulsion interface. Moreover, calcination could also eliminate organic compounds found inside the capsules. Given these constraints, the only way to modify the porosity of Pickering emulsion templated silica capsules is to adjust the kinetics of the hydrolysis and condensation reactions in the sol–gel process (Scheme 1).[29,30]

pH is a critical parameter controlling hydrolysis and condensation kinetics through modification of reaction mechanisms. Acidic conditions (pH < 2, below the isoelectric point of silica) favor hydrolysis over condensation, producing linear polymeric structures with microporous dense networks (Fig. 1), while alkaline conditions (pH > 7) promote rapid condensation yielding highly branched, more porous structures.[31–33] The hydrolysis rate exhibits a minimum at pH = 7 and increases exponentially at both lower and higher pH values, whereas condensation shows a minimum at pH = 2 and a maximum around pH = 7.[32] The H_2O/alkoxysilane molar ratio (R) strongly influences both reaction kinetics and final textural properties, with the stoichiometric requirement being $R = 4$ for complete hydrolysis.[34,35] Low R values ($\ll 4$) result in incomplete hydrolysis with more open, less crosslinked structures, while $R \gg 4$ promotes the formation of highly branched, polymerized networks with increased porosity.[34,35] Temperature accelerates both hydrolysis and condensation reactions but has complex effects on the final structure

$$\equiv\text{Si-OR} + H_2O \leftrightharpoons \equiv\text{Si-OH} + \text{R-OH}$$
(a) Alkoxysilane hydrolysis reaction.

$$\equiv\text{Si-OH} + \text{HO-Si}\equiv \leftrightharpoons \equiv\text{Si-O-Si}\equiv + H_2O$$
(b) Condensation reaction of silanols.

$$\equiv\text{Si-OR} + \text{HO-Si}\equiv \leftrightharpoons \equiv\text{Si-O-Si}\equiv + \text{R-OH}$$
(c) Condensation reaction of silanols and alkoxysilane.

Scheme 1 Reactions involved in the sol–gel process of silica with alkoxysilanes.

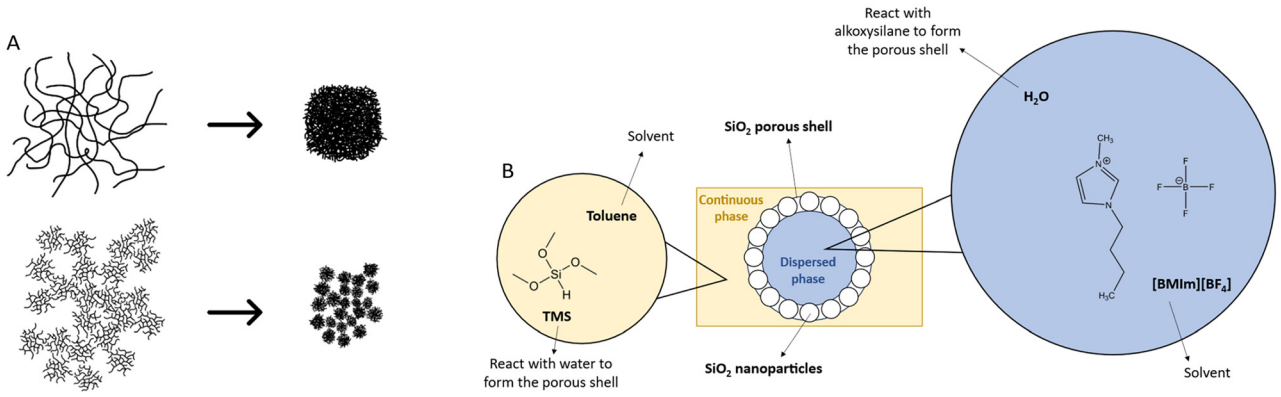

Fig. 1 (A) Schematic representation of the drying of silica gels under acid (top) and base catalysis (bottom). (B) General description of the system and composition of each phase.

depending on the sol–gel stage.[36,37] Higher gelation temperatures (50 °C) reduce gelation time but can cause solvent expulsion and network shrinkage, while aging temperature influences dissolution–reprecipitation mechanisms and neck formation between particles.[36,37] The reaction time also influences the hydrolysis and condensation processes in the sol–gel synthesis of silica. Longer hydrolysis and condensation times promote greater network connectivity and crosslinking, leading to densification of the silica matrix: ongoing condensation and Ostwald ripening progressively increase pore size but generally decrease the surface area and pore volume, as smaller pores collapse or merge.[38,39] Thus, shorter times favor a high surface area and mesoporosity.

Despite significant advances in silica capsule synthesis and growing interest in IL-containing materials, a systematic understanding of how synthesis parameters influence the textural properties and structural integrity of silica capsules prepared *via* Pickering emulsion templating remains limited. Furthermore, the impact of drying methods on capsule morphology has been underappreciated, especially when studying a material that is not meant to be dried, with most studies employing conventional drying, despite evidence of significant structural collapse due to capillary forces during solvent evaporation. The present work addresses these knowledge gaps through a comprehensive investigation of silica-based capsules containing ionic liquids synthesized *via* Pickering emulsion-templated sol–gel chemistry. Specifically, we examine how key synthesis parameters—including reaction temperature, reaction time, pH and water-to-alkoxysilane molar ratio—influence the textural properties (specific surface area, pore volume, and pore size distribution) and morphology of the resulting capsules. Particular emphasis is placed on the important role of supercritical CO_2 drying in preserving the inherent porosity of silica shells, with comparative analysis against conventional ambient pressure drying revealing substantial losses in microporosity and mesoporosity due to silica gel shrinkage. Through systematic variation of synthesis conditions combined with comprehensive structural characterization *via* nitrogen physisorption, scanning electron microscopy, and optical microscopy, we establish structure–property relationships that enable rational design of silica capsules with tailored textural features. The insights gained advance fundamental understanding of sol–gel chemistry at Pickering emulsion interfaces and provide practical guidance for engineering silica-based capsular materials for different applications. Moreover, this work demonstrates the feasibility of encapsulating ionic liquids within porous silica shells, creating a platform for developing functional materials that synergistically combine the unique properties of both components.

2. Experimental

2.1 Synthesis of the capsules

1-Butyl-3-methylimidazolium tetrafluoroborate [BMIm][BF_4] and deionized water were added to a 50 mL beaker. Homemade hydrophobized spherical silica nanoparticles (further details on the synthesis of these nanoparticles are provided in the SI) and 10 mL of toluene were added to another 50 mL beaker and predispersed using an ultrasonic bath for 2–3 min. The nanoparticles were then dispersed using an Ultra-Turrax IKA T-25 at 12 000 rpm for 15 s, and the entire mixture from the other beaker was added dropwise while maintaining stirring. The mixture was then stirred for 1.5 minutes until an emulsion was formed, which was subsequently transferred to a 250 mL double-jacketed reactor. A solution of trimethoxysilane (TMS) in toluene was also added, and the mixture was stirred at 150 rpm using a motor and an inclined-blade turbine stirrer for a specified time and at a specified temperature. The TMS and the water contained in the emulsion droplets react *via* an interfacial polycondensation sol–gel process to form a silica gel shell around the emulsion droplets. Fig. 1 shows a schematic description of the system's composition. A summary diagram of the synthesis is given in Fig. S6 and the details of all experimental conditions for the syntheses are provided, respectively, in Table S1.

2.2 Washing of the capsules

After the reaction, the mixture was transferred to a 250 mL separatory funnel, and the capsules were washed twice with 50 mL of toluene. After sedimentation, the capsules were transferred to a 50 mL glass vial and washed with 6 × 30 mL of acetone, allowing them to settle and removing as much supernatant as possible between each step.

2.3 Drying of the capsules

Once the acetone washing steps were completed, the capsules were divided into two batches: one was dried at room temperature and pressure in a crystallizing dish, and the other was dried using supercritical CO_2.

Room temperature and pressure drying. As much supernatant as possible was removed after the capsules had settled and then they were transferred to a crystallizing dish under a fume hood and dried at room temperature and pressure for 4 h.

Supercritical CO_2 drying. A Leica EM CPD300 supercritical CO_2 dryer was used in combination with a specially designed and custom-machined sample holder, which allowed the capsules to be contained and prevented them from being dispersed in the drying chamber.

2.4 Characterization

The capsules were examined using SEM with a JEOL JSM-IT-800 microscope operated *via* SEM Center software. The capsules were also observed using an Olympus BX51 optical microscope equipped with an Olympus UC30 camera and controlled through Stream Essentials software. The average diameters and polydispersity of the observed objects were obtained using a Python script based on the Hough transform and the OpenCV package. More information on observation conditions and sample preparation is given in the SI. The tex-

tural properties of the capsules were determined using nitrogen physisorption. Samples were first degassed on a desorption apparatus, which consists of a vacuum manifold and tubular furnaces and can accommodate up to 8 analysis cells. The samples were then analyzed with a Micromeritics ASAP 2420 using N_2 at 77 K. Data were processed using MicroActive software and a Python script. The BET specific surface area (S_{BET}) was determined using the BET method assisted by the Rouquerol validation parameter; the mesopore size distribution and mesoporous volume (V_{meso}) were determined using the BJH method; and the micropore size distribution and microporous volume (V_{micro}) were determined using the HK method (confirmed by the DR method) with an adjusted adsorbate–adsorbent interaction parameter (more details are given in the SI). Further details on the principles of nitrogen physisorption and the various methods used are available in the SI. GC analyses were performed on an Agilent Technologies 6890N system equipped with a PONA column and an FID, operated *via* Chromeleon software.

3. Results and discussion

3.1 Description of capsules and reference

All capsules synthesized in this study had a diameter equal to approximately 15 μm (Fig. 2A). This diameter is constant across syntheses because it depends on the size of the Pickering emulsion droplets, which itself depends on the speed and duration of emulsification as well as the quantity of nanoparticles used, which were kept identical for each synthesis.

The capsule wall thickness is very difficult to quantify, particularly when the capsules are dried with supercritical CO_2. Since the walls are very thin and porous, the electron beam in SEM penetrates the shell—even at the lowest possible acceleration voltage on the SEM (1 kV)—and the shell appears translucent in SEM images (Fig. 2B). Moreover, the capsules must also be fractured, and the fractured piece must face the SEM detector, which makes the measurement tedious. Measurements were taken on capsules dried at room tempera-

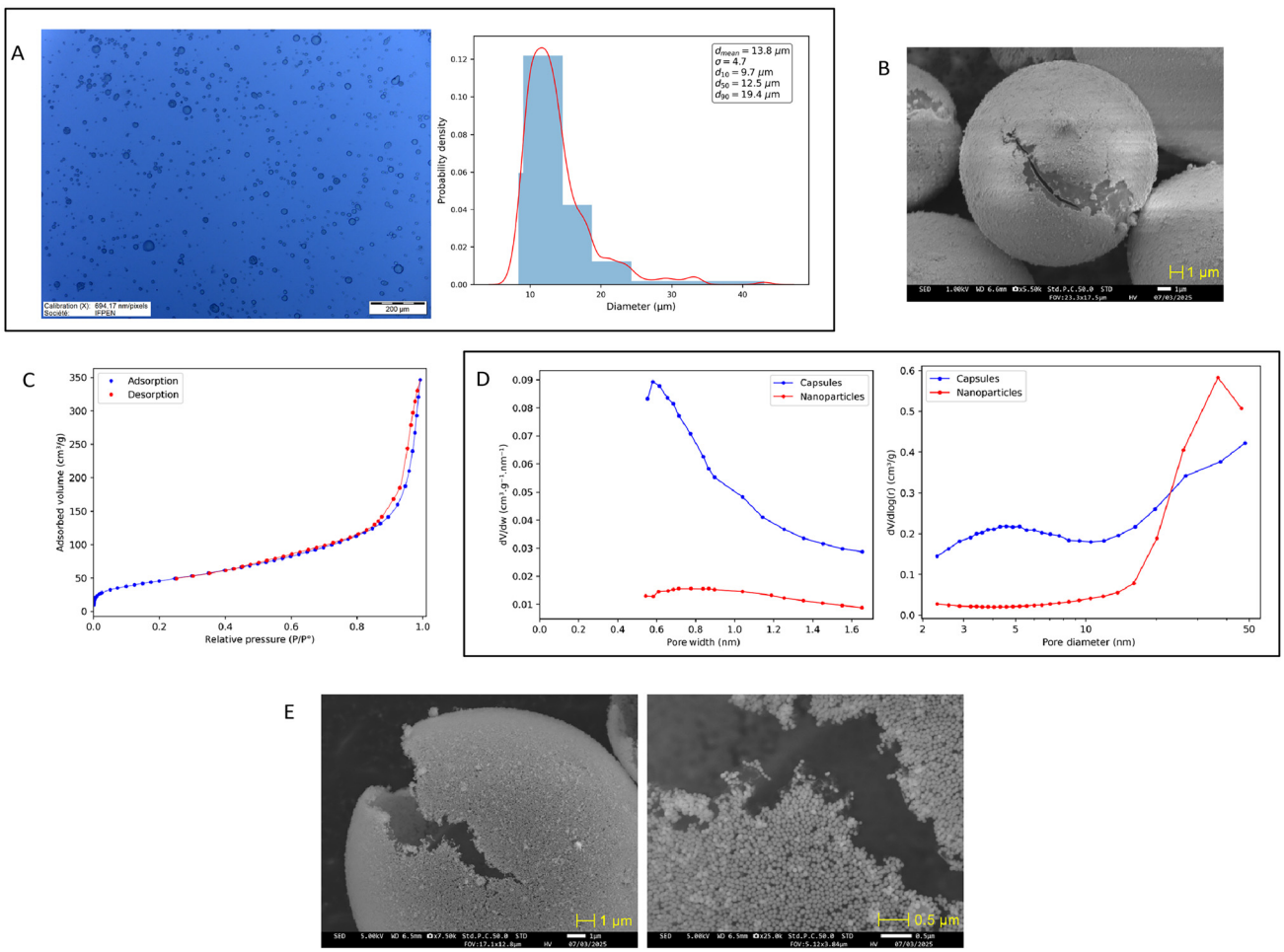

Fig. 2 (A) Optical microscopy image of capsules and diameter distribution from a Python script. (B) SEM image of a capsule. (C) Type II nitrogen physisorption isotherms with an H3 hysteresis loop of the capsules. (D) Size distributions of micropores (left) and mesopores (right) of capsules compared to the distributions of the nanoparticles used to make the Pickering emulsion. (E) SEM images of the spherical silica nanoparticles used to make the Pickering emulsion surrounding each capsule. The right image shows the left image at a higher magnification.

ture and pressure, which provides better contrast because the shells are less porous.

All nitrogen isotherms of the capsules obtained—whether dried at room temperature and pressure or with supercritical CO_2—were type II isotherms with an H3 hysteresis loop (Fig. 2C). A single batch of capsules was analyzed *via* nitrogen physisorption with an interval of several days to assess the reproducibility of the textural property analysis (see the SI). Reversible type II isotherms correspond to the physisorption of most gases on nonporous or macroporous adsorbents (in this case, macroporous, given the volume of gas adsorbed).[40] Here, the adsorption branch resembles a type II isotherm, but the desorption branch is not reversible and forms a hysteresis loop, more specifically H3. Such loops are characteristic of non-rigid aggregates of particles but also appear when the pore network consists of macropores that are not completely filled with condensate.[40] The H3 hysteresis loop may also be associated with slit-shaped pores,[41] and given the pH of the water–IL mixture used in the silica sol–gel reaction, which is acidic (pH = 3),[42,43] the resulting gel can be considered a polymeric gel,[44] forming a mostly microporous material with slit-shaped pores once dried.

Regarding the textural properties, the synthesis parameters studied and their associated ranges are as follows: reaction temperature (5 °C, 20 °C, and 50 °C), reaction time (6 h and 24 h), pH (pH = 0, pH = 3, and pH = 9), and R ratio (R = 0.5, R = 4, and R = 16). A reference synthesis was defined with "intermediate" parameters relative to all those studied (RD2: 20 °C, 6 h, pH = 3, R = 4). The mesopore and micropore size distributions are shown in Fig. 2D. The microporous volume originates entirely from the porous sol–gel shell because nanoparticles have little to no volume in this range as shown by the micropore size distribution. Regarding the mesoporous volume, the results are more nuanced. Indeed, it appears that the nanoparticles' mesoporous volume increases starting from 12 nm and reaches a peak at approximately 45 nm. This porous volume is induced by the interparticle void between the spherical nanoparticles. In the case of a random, uncompressed packing of solid polydisperse spheres whose diameters follow a log–normal distribution with a standard deviation σ = 0.3 and a mean diameter d, and knowing that the packing density is φ = 0.61,[80] the effective average pore diameter induced by the packing is given by $d_{pores} = 0.572 \times d_{nanos}$.[46] Given that the nanoparticles have an average diameter of 80 nm (see the SI), this results in a theoretical pore diameter of 46 nm, which corresponds exactly to what is observed in the mesopore size distribution. Unfortunately, this porous volume originating from the nanoparticles between 12 and 50 nm is reflected in the mesopore size distribution of the capsules, where an increase in mesoporous volume is observed starting from approximately 12 nm. It would be possible to determine the theoretical diameter of the spherical nanoparticles so that the porosity generated by the interparticle space exceeds 50 nm. Assuming that the nanoparticles assemble into a compact 2D hexagonal packing on the surface of emulsion droplets (which appears to be the case according to the SEM images, Fig. 2E), the pore diameter induced by the assembly is $d_{pores} = 0.3094 \times d_{nanos}$.[48] Thus, the nanoparticles should have a diameter of

$$d_{nanos} > \frac{d_{pores}}{0.1547} = \frac{50}{0.3094} = 162\,\text{nm}$$

Unfortunately, it was difficult to stabilize the Pickering emulsions with nanoparticles that had too large a diameter, and a theoretical calculation determined that the ideal size was around 80–100 nm (see the SI). Therefore, nanoparticles with an average diameter of 80 nm were synthesized. Hence, two areas have been defined: a first one between 2 and 12 nm, where the mesoporosity is entirely induced by the sol–gel shell, and another between 12 and 50 nm, where the mesoporosity originates from both the nanoparticles and the sol–gel shell, but where it is not possible to clearly define the contribution of each material. All mesopore size distributions as well as mesoporous volumes in the remainder of this paper have been detailed based on these two areas.

3.2 Supercritical CO_2 drying

Silica gels undergo a certain amount of shrinkage during drying, even at room temperature and pressure, mainly due to capillary forces generated at the liquid–vapor interface within the porous structure.[45,47,49,50] Drying begins with the formation of a meniscus at the outer surface of the pores. This liquid–vapor interface is subjected to capillary pressure, and the tension of the liquid confined within a cylindrical pore of radius r_c (m) can be calculated using the Young–Laplace equation:

$$\Delta p = \frac{2\gamma_{LV}\cos(\theta)}{r_c} \quad (1)$$

where Δp is the capillary pressure (Pa), γ_{LV} the surface tension at the liquid–vapor interface (N m^{-1}), and θ the contact angle of the meniscus (radian). When the meniscus reaches smaller pores, the liquid tension increases, inducing compressive forces on the solid matrix that may exceed its elastic limit and damage the material's structure.[50] These stresses, which can exceed 100 MPa, lead to a decrease in the pore volume of a silica gel during drying, ranging from a few percent to more than 50%, depending on the drying conditions.[45,47,49–51]

However, the deformations and cracks often observed during drying do not depend on the absolute value of the stress.[50] If the stress were hydrostatic, the matrix would contract isotropically, and no damage would occur. It is the capillary pressure gradient within the pores that causes differential contraction and, consequently, mechanical damage to the network.[50] This shrinkage and mechanical damage to the silica gel structure result in the collapse of the capsules upon drying (Fig. 3A).

The capsules dried at ambient temperature are therefore not representative of the actual system because they are not meant to be dried but rather used while still suspended in a solvent; their textural properties are lower than the real values due to shrinkage; they do not retain their original shape during drying (collapse upon themselves).

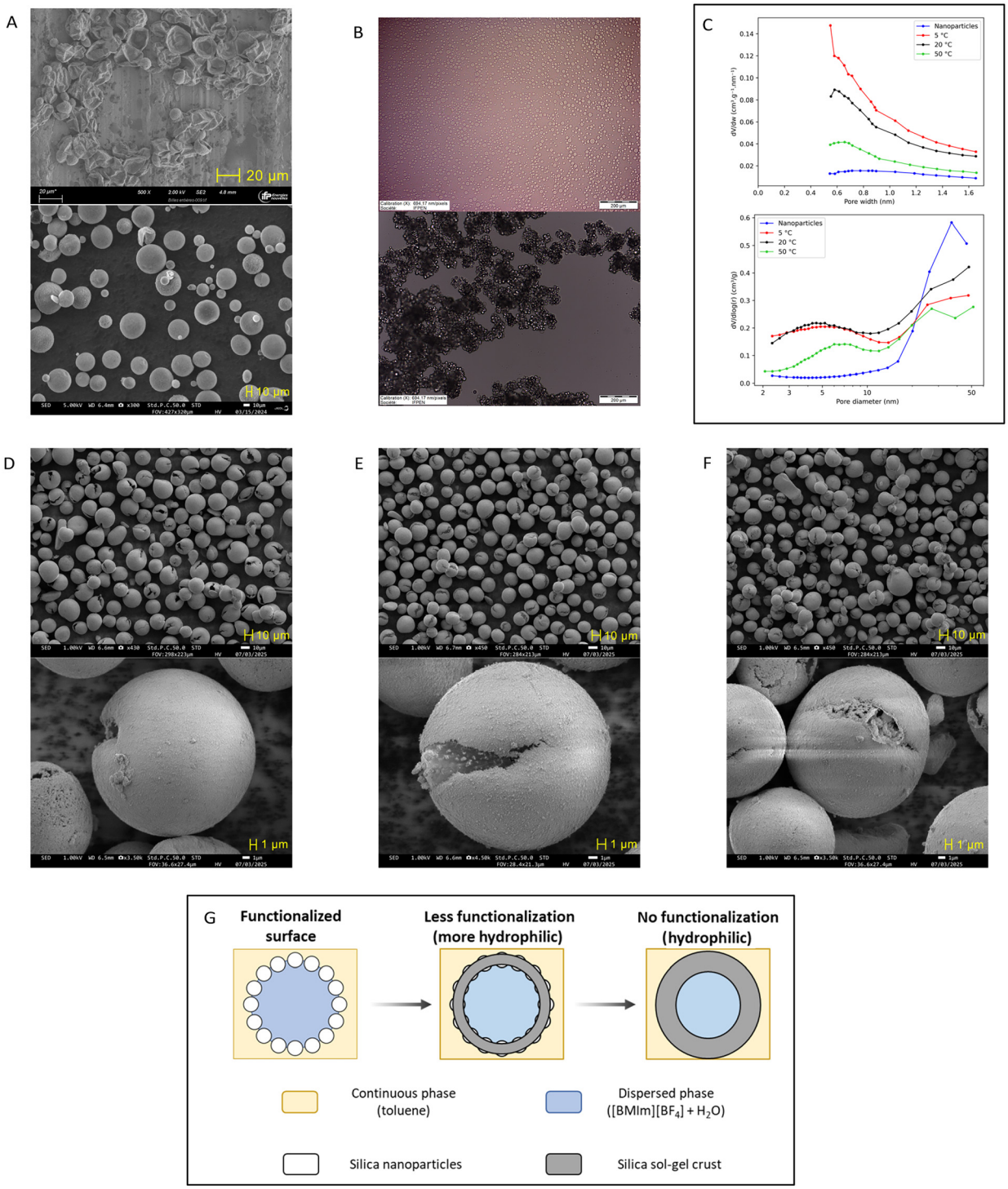

Fig. 3 (A) Comparison between capsules dried at ambient temperature and pressure (top) and with supercritical CO_2 (bottom) in SEM. (B) Optical microscopy images of dispersed (top) and flocculated (bottom) capsules. (C) Size distributions of micropores (top) and mesopores (bottom) of capsules synthesized at different temperatures compared to the distributions of the nanoparticles used to make the Pickering emulsion. (D) SEM images of capsules synthesized at 5 °C. (E) SEM images of capsules synthesized at 20 °C. (F) SEM images of capsules synthesized at 50 °C. (G) Schematic of sol–gel shell growth over hydrophobized silica nanoparticles.

Alternative drying methods can be used to address this issue: lyophilization and supercritical CO_2 drying. However, supercritical CO_2 drying is preferable in this case because lyophilization requires a solvent exchange (most lyophilizers are only compatible with water), and the solidification of water leads to a volume expansion that creates a stress gradient in

the silica gel from the outside inward,[52] resulting in effects similar to those observed with ambient temperature and pressure drying (shrinkage, reduction in pore volume, deformation, cracks), although to a lesser extent. Furthermore, the capsules are hydrophobic (due to the surface functionalization of the nanoparticles used for the Pickering emulsion, which remains present), making it impossible to disperse them in water.

Supercritical CO_2 drying eliminates the capillary pressure generated at the liquid–vapor interface by gradually replacing the solvent in which the silica gel is suspended (here, acetone) with liquid CO_2 through several successive washings. Once the initial solvent is completely replaced with liquid CO_2, the temperature and consequently the pressure are increased until the supercritical state is reached (31.1 °C and 73.8 bar for CO_2). The pressure is then gradually reduced at constant temperature to transition directly from the supercritical to the gaseous state, thus preventing the formation of a liquid–vapor interface and the associated capillary forces. Indeed, supercritical CO_2 has zero surface tension, and since stresses are governed by the Young–Laplace equation, eliminating surface tension nullifies capillary pressure. This drying step is necessary for capsule characterization but is not part of the synthesis process (as a reminder, the capsules are not intended to be dried but used as-is after synthesis).

A comparative study of the textural properties of 16 different batches of capsules – which were split in two and dried by two different methods: at ambient temperature and pressure and using supercritical CO_2 – was carried out. These syntheses were carried out using the following ranges of operating conditions: reaction temperature∈[5; 20; 50] °C, reaction time∈[6; 24] h, pH∈[0; 3; 9], and R ratio∈[0.5; 4; 16]. Average values of textural properties (and standard deviations) are provided in Table 1.

The BET surface area (S_{BET}) and microporous volume (V_{micro}) followed identical trends for each sample (as S_{BET} is primarily driven by V_{micro}), with an average loss due to ambient temperature/pressure drying of −45.8% for S_{BET} and −46.6% for V_{micro} (Table 1). Among all samples, the loss due to ambient drying ranged from −12.7% to −71.9% for S_{BET} and from −13.2% to −71.7% for V_{micro}. This variability is due to structural differences in the silica gel prior to drying, which vary between samples.

As for the mesoporous volume (V_{meso}), a loss was observed across all samples except for one ranging from −1.5% to −49.7%, with an average of −17.6%. The mesopores were divided into two distinct ranges based on the influence of Pickering emulsion nanoparticles on the textural properties of the capsules (further explanations are given in the next section): "small" mesopores between 2 and 12 nm and "large" mesopores between 12 and 50 nm. A loss of porosity in the small mesopore range was observed in all samples, varying from −9.3% to −62.1%, with an average of −39.5%. For the large mesopores, the variation was entirely random (pore volume increased or decreased depending on the sample, with no clear correlation to the experimental conditions of those samples), ranging from −48.1% to 40.3%, with an average of −2.9%.

This study demonstrated the necessity of using supercritical CO_2 drying for the investigation of the capsules' textural properties, as drying at ambient temperature and pressure leads to an overall loss of porosity due to silica shrinkage. Throughout the remainder of this paper, all textural properties are reported following supercritical CO_2 drying.

3.3 Influence of reaction temperature

During the study of the sol–gel reaction temperature, issues of flocculation and sedimentation of the capsules during the encapsulation phase in the double-jacketed reactor were observed after a few hours. The flocculated and sedimented capsules were examined under optical microscopy and compared to well-dispersed capsules (Fig. 3B). The hypothesis proposed to explain the cause of this phenomenon is the following: the surface chemistry of the capsules is altered during interfacial polycondensation because the shell formed by the sol–gel reaction grows over the hydrophobized nanoparticles over time, preventing the capsules from remaining well dispersed in toluene, as the silica formed is hydrophilic (Fig. 3G). To confirm this hypothesis, three capsule syntheses were carried out under the same experimental conditions but at three different temperatures: 5 °C (RD1), 20 °C (RD2), and 50 °C (RD3). The textural properties are provided in Table 2 and the mesopore and micropore size distributions are shown in Fig. 3C.

At 5 °C, there was no flocculation or sedimentation. At 20 °C, the capsules slightly began to flocculate after 6 h.

Table 1 Average values (and standard deviations) of the textural properties of 16 different batches of capsules dried at ambient temperature and pressure and with supercritical CO_2

	S_{BET} ($m^2\ g^{-1}$)	V_{meso} total ($cm^3\ g^{-1}$)	V_{meso} 2–12 nm ($cm^3\ g^{-1}$)	V_{meso} 12–50 nm ($cm^3\ g^{-1}$)	V_{micro} ($cm^3\ g^{-1}$)
T_{amb}/P_{amb}	99 (24)	0.245 (0.069)	0.067 (0.024)	0.175 (0.053)	0.041 (0.010)
sCO_2	192 (76)	0.309 (0.121)	0.117 (0.063)	0.190 (0.079)	0.081 (0.032)
Difference	−45.8%	−17.6%	−39.5%	−2.9%	−46.6%

The difference represents the gap between the textural properties of the capsules dried with supercritical CO_2 (the actual textural properties of the material) and the textural properties of the same capsules dried at room temperature and pressure, corresponding to the loss (or gain) of porosity resulting from drying under ambient conditions. It is expressed here as a geometric mean based on the data from Table S3. The values for T_{amb}/P_{amb} and sCO_2 are averages.

Table 2 Textural properties of the first capsules at different reaction temperatures

Sample	S_{BET} ($m^2\ g^{-1}$)	V_{micro} ($cm^3\ g^{-1}$)	V_{meso} total ($cm^3\ g^{-1}$)	V_{meso} 2–12 nm ($cm^3\ g^{-1}$)	V_{meso} 12–50 nm ($cm^3\ g^{-1}$)
5 °C (RD1)	209	0.089	0.316	0.144	0.172
20 °C (RD2)	168	0.071	0.358	0.149	0.209
50 °C (RD3)	81	0.034	0.232	0.082	0.122

Fixed parameters: 6 h; pH = 3; R = 4.

Finally, at 50 °C, the capsules began to flocculate after 4 h and were completely flocculated and sedimented within 6 h.

Regarding the textural properties, Table 2 shows the S_{BET} and the V_{micro} decrease as the reaction temperature increases. This result is even more striking in the micropore size distributions (Fig. 3C), where the curve at 5 °C lies above that at 20 °C across the entire micropore range, which itself lies above the curve at 50 °C across the entire range. For the mesopores, there is a slight increase in V_{meso} when moving from 5 °C to 20 °C, followed by a drastic decrease—well below the V_{meso} at 5 °C—when the reaction temperature reaches 50 °C. Examining the mesopore size distributions (Fig. 3C) in more detail, one can see that the difference in V_{meso} between the 5 °C and 20 °C syntheses occurs mainly in the large mesopores between 10 and 50 nm; the two curves almost overlap between 2 and 10 nm. This may be due to a slight variability in the initial nanoparticle coverage of the emulsion droplets, since the mesoporous volume between 10 and 50 nm is partly induced by the space between the nanoparticles. At 50 °C, however, the curve lies below that of 20 °C across the entire mesopore domain and below that of 5 °C mainly in the 2 to 20 nm range.

The comparison between the micropore and mesopore size distributions of the nanoparticles and those of the capsules at different temperatures shows that the microporosity entirely originates from the sol–gel shell, as do the mesopores between approximately 2 and 12 nm. From around 20 nm upward, the capsule distributions fall below those of the nanoparticles, which can imply several things: the sol–gel shell fills the pores induced by the nanoparticles; the nanoparticles are no longer in the form of a random 3D packing of polydisperse solid spheres but rather as a compact 2D hexagonal arrangement in a plane, which causes a change in the pore size induced by the packing.

The textural properties of the synthesized capsules are consistent with literature findings: even in the absence of supercritical CO_2 drying, an increase in gelation temperature correlates with a decrease in micropore volume.[53–57] This trend results from kinetic and structural variations in sol–gel polymerization. At low temperatures, slower polycondensation allows silica to form numerous small nuclei that assemble into a branched network with very small inter-particle voids. Conversely, higher temperatures accelerate hydrolysis and condensation, leading to the rapid growth of silica aggregates that freeze into coarser structures, thereby hindering micropore formation.[12,13] Regarding mesoporosity, the evolution of V_{meso} as a function of temperature is non-linear due to competing physicochemical processes, resulting in a network that is predominantly microporous with a smaller mesoporous contribution.[36,54,58] At ambient temperature, reaction kinetics accelerate sufficiently to shorten gelation time while permitting structural rearrangements; this yields a more open structure with thicker shells and numerous mesopores derived from interconnected primary particles or spinodal voids.[59] However, at elevated temperatures, the network "freezes" prematurely due to drastic kinetic acceleration, halting the development of any meso- or macroporous network.[36] Consequently, the silica precipitates as densely fused particles where micropores merge or vanish, resulting in a compact and less porous shell.[55]

The capsules synthesized at 5 °C, 20 °C and 50 °C were also analysed by SEM (Fig. 3D, E and F). However, it is difficult to draw conclusions from these images because even at the lowest possible acceleration voltage on the SEM (1 kV), the electron beam penetrated the shell, which is extremely thin and porous, and the shell appears as a translucent veil in the images. Consequently, it is not really possible to quantify how much the shell covers the nanoparticles.

Despite supercritical CO_2 drying, all shells—regardless of temperature—appear to be split open, yet they maintain a spherical shape. The rapid evacuation to vacuum before SEM observation may have caused the capsules to burst and split. Simply draining their liquid and drying them, even with supercritical CO_2, may also be sufficient. The capsules synthesized at 5 °C appear to have smoother surfaces and fewer small fragments than the others. Moreover, the split edges of the capsules synthesized at 5 °C seem to close in on themselves, unlike those of the capsules at the other two temperatures, which retain their shape—this could indicate a more flexible shell and therefore one that is more porous and/or thinner. Indeed, there are far more capsule fragments scattered in the case of the capsules synthesized at 50 °C, which indicates that the capsules are more rigid and fracture rather than deform. This might indicate a thicker and/or a denser shell.

Two phenomena are involved in explaining these differences in rigidity. First, in porous materials, increasing density (*i.e.*, decreasing porosity) strengthens the structure, leading to a higher Young's modulus.[36] Second, flexural rigidity is proportional to the cube of the thickness according to Kirchhoff–Love theory, so a shell thickness twice as large will yield a capsule eight times more rigid.[37,60] The critical buckling load is proportional to thickness squared; therefore, a shell twice as thick will require four times more force to buckle.[37,60] Generally speaking, the capsules synthesized at 20 °C show the least damage and the most spherical shape, which could be explained by a compromise between the material's porosity and the shell thickness.

All these results also confirm the previously stated hypothesis: the shell formed by the sol–gel reaction grows over the functionalised nanoparticles over time, which prevents the capsules from staying well dispersed in toluene after a certain time.

3.4 Influence of reaction time

The influence of reaction time on the textural properties of the capsules was studied, as well as its role in the flocculation and sedimentation phenomena described previously. Two syntheses were therefore carried out: one with a reaction time of 6 h (RD2) and the other with a reaction time of 24 h (RD4). The textural properties of capsules are given in Table 3. The mesopore and micropore size distributions are displayed in Fig. 4A.

After 6 h of reaction, the capsules remained well dispersed, but after 24 h, they were completely flocculated and sedimented as expected. The S_{BET}, V_{micro} and V_{meso} of the 24 h capsules are all lower than those of the 6 h capsules (Table 3). Examining the micropore and mesopore size distributions (Fig. 4A) shows that while the profiles are similar, the 24 h curves lie below the 6 h curves across the entire micropore and mesopore ranges. The results mirror those obtained for capsules synthesized at different reaction temperatures: the microporosity originates entirely from the sol–gel shell, as do the mesopores between 2 and 12 nm; beyond around 12–50 nm, the mesopore volume appears to derive partly from nanoparticle reorganisation and partly from the sol–gel shell.

Extending the reaction time allows a more complete condensation of the silica networks, and the results are comparable to those observed with increasing temperature. Two phenomena influence the evolution of V_{micro} and V_{meso} over time. Increasing the reaction duration allows more terminal Si–OH and Si–OH or Si–OR groups to condense into ≡Si–O–Si≡ bonds. This reinforces network cross-linking and often causes network contraction (syneresis), which brings structural units closer together, expels solvent from pores, and increases the skeletal density of the solid matrix.[61] The micropores are the first to be eliminated by this process, because they are tiny voids that can be filled or reduced as the structure reorganises.

Table 3 Textural properties of capsules at different reaction times

Sample	S_{BET} ($m^2\ g^{-1}$)	V_{micro} ($cm^3\ g^{-1}$)	V_{meso} total ($cm^3\ g^{-1}$)	V_{meso} 2–12 nm ($cm^3\ g^{-1}$)	V_{meso} 12–50 nm ($cm^3\ g^{-1}$)
6 h (RD2)	168	0.071	0.358	0.149	0.209
24 h (RD4)	126	0.053	0.293	0.120	0.173

Fixed parameters: 20 °C; pH = 3; R = 4.

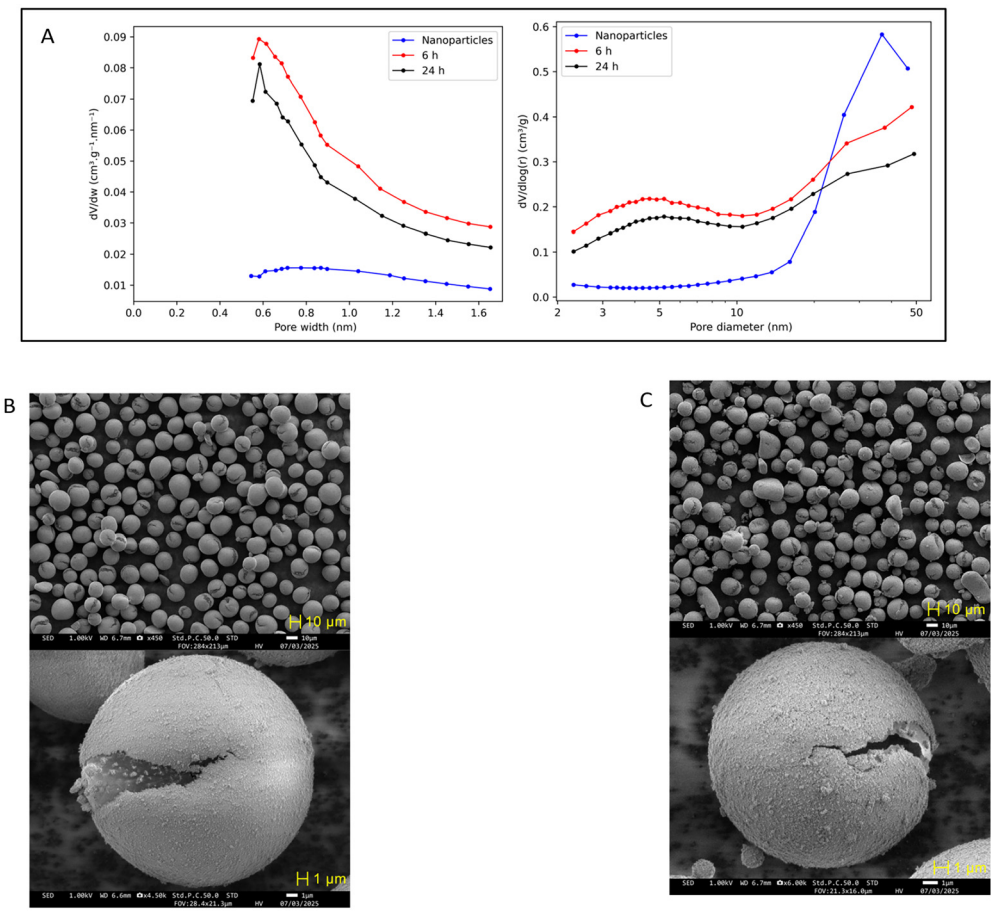

Fig. 4 (A) Size distributions of micropores (left) and mesopores (right) of capsules synthesized at different reaction times compared to the distributions of the nanoparticles used to make the Pickering emulsion. (B) SEM images of capsules synthesized during 6 h. (C) SEM images of capsules synthesized during 24 h.

This explains why micropore volume decreases with reaction time in silica gels. The evolution of mesoporous volume with reaction time is more nuanced and depends strongly on the experimental conditions of the synthesis, because syneresis competes with another phenomenon: Ostwald ripening. In this dissolution–reprecipitation phenomenon, silica from convex surfaces (positive curvature) dissolves to reprecipitate on concave surfaces (negative curvature).[61] Ostwald ripening for silica depends mainly on pH: at acidic or neutral pH (which is the case for the capsule syntheses at 6 h and 24 h), the solubility of silica is low or zero, so Ostwald ripening is negligible and it is the syneresis induced by polycondensation that dominates, which causes V_{micro} as well as V_{meso} to decrease as reaction time increases; at basic pH, silica becomes partially soluble and Ostwald ripening then occurs, which causes the disappearance of micropores and small mesopores in favour of larger mesopores.[61]

The capsules were also analysed by SEM (Fig. 4B and C). The capsules after 24 h of reaction are all split open, as in the previous study on reaction temperature. Furthermore, a large amount of scattered capsule debris is visible after 24 h of reaction, in contrast to the 6 h samples. This brittle behavior implies that the capsules are more rigid and prone to fracture instead of deformation, potentially due to an increased shell thickness or density.

3.5 Influence of pH

The pH of the dispersed phase is a very important parameter in silica sol–gel chemistry because it greatly impacts the kinetics of hydrolysis and condensation reactions as well as the dissolution–precipitation process. Three syntheses were therefore carried out: one at acidic pH (pH = 0) by replacing water with a 1 mol L^{-1} HCl solution (RD5), one at basic pH (pH = 0) by replacing water with 20.5% ammonia (RD6), and one at moderately acidic pH (pH = 3) using water (RD2). The synthesis using only water does not have a neutral pH because [BMIm][BF_4] possesses slight acidity in the presence of water.[42] These pH values were measured with a pH meter and confirmed with pH paper. The textural properties are given in Table 4 and the pore size distributions of the mesopores and micropores in Fig. 5A.

The capsules obtained at pH = 0 and pH = 3 remained well dispersed after 6 h of reaction, whereas the capsules at pH = 9 were completely flocculated and sedimented after only 1.5 h of reaction. The S_{BET} and V_{micro} are minimal at pH = 3 (S_{BET} = 168 m^2 g^{-1}; V_{micro} = 0.071 cm^3 g^{-1}) and increase at pH = 0 (S_{BET} = 273 m^2 g^{-1}; V_{micro} = 0.116 cm^3 g^{-1}) and pH = 9 (S_{BET} = 221 m^2 g^{-1}; V_{micro} = 0.093 cm^3 g^{-1}), with maxima at pH = 0 (Table 4). The micropore size distributions show that the curves at pH = 0 and pH = 9 are higher than that at pH = 3 over the entire micropore domain, with the curve at pH = 0 dominating. Regarding mesopores, the V_{meso} of the capsules at pH = 0 (V_{meso} = 0.509 cm^3 g^{-1}) is far higher than at pH = 3 (V_{meso} = 0.358 cm^3 g^{-1}) and pH = 9 (V_{meso} = 0.366 cm^3 g^{-1}). The mesopore size distributions show that the distributions are more or less identical from 2 to 6 nm and that the main differences lie between 6 and 50 nm: the curve of the capsules at pH = 0 is markedly higher than the other two in that domain. The curve at pH = 9 is slightly higher than the one at pH = 3 between 6 and 30 nm and then falls again from 30 nm to 50 nm, whereas the curve at pH = 3 continues to increase in that range. Compared with the mesopore size distribution of the nanoparticles used to form the Pickering emulsion, acidic catalysis appears to generate a sol–gel shell that is more open and more porous than the other two pH conditions.

Table 4 Textural properties of capsules at different pH values

Sample	S_{BET} (m^2 g^{-1})	V_{micro} (cm^3 g^{-1})	V_{meso} total (cm^3 g^{-1})	V_{meso} 2–12 nm (cm^3 g^{-1})	V_{meso} 12–50 nm (cm^3 g^{-1})
pH = 0 (RD5)	273	0.116	0.509	0.176	0.332
pH = 3 (RD2)	168	0.071	0.358	0.149	0.209
pH = 9 (RD6)	221	0.093	0.366	0.160	0.206

Fixed parameters: 6 h; 20 °C; R = 4.

In acid catalysis, the hydrolysis reaction is fast and condensation is slower. The Si–OH groups are protonated and the slow condensation forms linear or randomly branched polymers rich in silanol groups, which gradually entangle to form a polymeric gel (Fig. 1A).[62–67] In base catalysis, condensation is faster than hydrolysis. The silanols are deprotonated, which leads to the formation of more highly branched aggregates, which do not interpenetrate before gelation and behave like discrete species, forming a colloidal gel (Fig. 1A).[62–67] At neutral pH, hydrolysis is very slow and particle growth is therefore gradual. The structure of the resulting gel is therefore intermediate between a polymeric gel and a colloidal gel.[66]

As mentioned earlier, the textural properties depend strongly on how the silica gel was dried. Thus, during conventional drying, the polymeric gel formed under acid catalysis will collapse on itself due to silica shrinkage to form a primarily microporous material.[5,68–71] The colloidal gel formed under base catalysis retains larger inter-particle voids during drying and silica shrinkage, leading to a rather mesoporous material.[5,68–71] However, the capsules were dried using supercritical CO_2, bringing them closer to an aerogel-type structure and preserving a structure more akin to the gel before drying. The capsules formed under acid catalysis thus have a much more porous structure than under base catalysis,[62,68,72,73] which could explain why capsules formed under acid catalysis have a much larger mesopore volume. The fact that the mesopore size distributions of capsules at pH = 3 and pH = 9 are similar can be explained by the fact that the silica polymerisation process is divided into two distinct domains that depend on the isoelectric point of silica, which is at pH = 2.[74] The mechanism of silica condensation is therefore similar for all gels produced at pH > 2.[74]

The capsules were also analysed by SEM (Fig. 5B–D). The capsules synthesised at pH = 0 also appear split open but retain their spherical shape. The split contours seem to fold in on themselves (like the capsules synthesised at 5 °C, but even

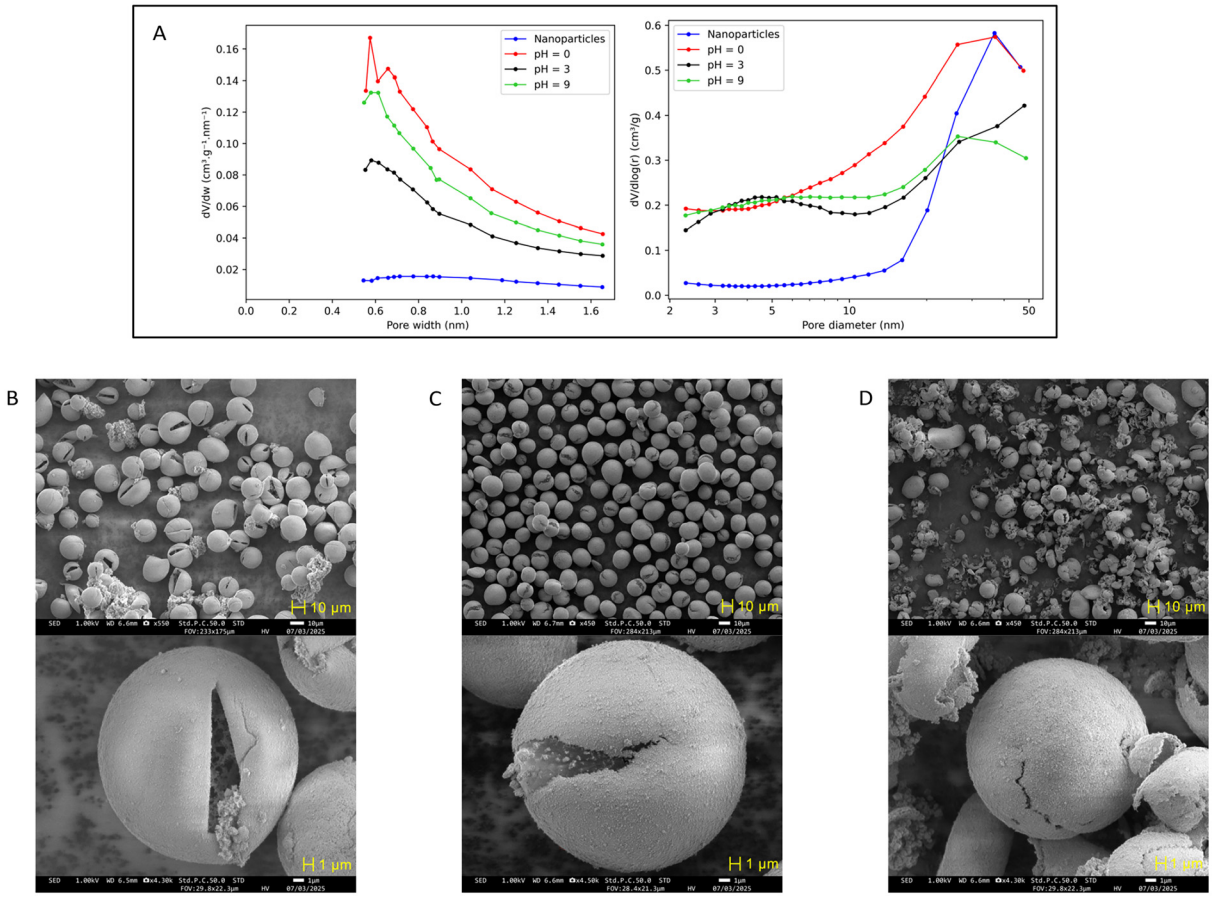

Fig. 5 (A) Size distributions of micropores (left) and mesopores (right) of capsules synthesized at different pH values compared to the distributions of the nanoparticles used to make the Pickering emulsion. (B) SEM images of capsules synthesized at pH = 0. (C) SEM images of capsules synthesized at pH = 3. (D) SEM images of capsules synthesized at pH = 9.

more markedly) unlike the capsules synthesised at pH = 3, which could indicate a more flexible shell, *i.e.*, more porous and/or thinner. It is also possible to observe silica aggregates inside the capsules synthesised at pH = 0 but also outside. The capsules synthesised at pH = 9 did not retain their structural integrity and are for the most part completely broken into pieces. The capsules appear rigid, as the fragments retained the curvature of the original capsule. These differences can be explained by the structural difference between each sample: the shell of the capsules under acid catalysis is formed of long linear or randomly branched polymers that entangle, which results in a cohesive gel with some flexibility; the shell of the capsules under base catalysis is formed of more highly branched aggregates that do not interpenetrate before gelation and behave as discrete species, which gives a less cohesive and more rigid gel, hence more prone to breaking. Moreover, condensation is increasingly advanced as pH increases and it was previously mentioned that the more advanced the condensation, the more the shell's porous network densifies, which results in increased rigidity. Concerning the silica aggregates inside the capsules at pH = 0, since hydrolysis is very rapid and condensation slow, the silica oligomers have time to move within the dispersed phase and do not necessarily condense only at the interphase but also inside the capsules.

3.6 Influence of the H_2O/alkoxysilane molar ratio

The molar ratio R between water and the alkoxysilane is also a parameter that strongly influences silica sol–gel chemistry. The stoichiometry of the reaction depends on the number of alkoxy groups bound to Si, as shown in Scheme 1. Thus, for alkoxysilanes with four Si–OR bonds to hydrolyse, such as TEOS, stoichiometry between water and alkoxysilane is satisfied when R = 4. In the case of TMS, used for all the capsule syntheses thus far, it is composed of three Si–O–CH_3 bonds and one Si–H bond. The Si–H bond can hydrolyse and form a silanol according to the reaction shown in Scheme 2.

However, this reaction is not kinetically favourable and depends on the pH of the water: a basic pH greatly favours the reaction, unlike neutral or acidic pH.[75–77] Thus, the stoichio-

$$\equiv\text{Si-H} + H_2O \leftrightharpoons \equiv\text{Si-OH} + H_2$$

Scheme 2 Hydrolysis reaction of the Si–H bond of TMS.

Table 5 Textural properties of capsules at different R ratios

Sample	S_{BET} ($m^2\ g^{-1}$)	V_{micro} ($cm^3\ g^{-1}$)	V_{meso} total ($cm^3\ g^{-1}$)	V_{meso} 2–12 nm ($cm^3\ g^{-1}$)	V_{meso} 12–50 nm ($cm^3\ g^{-1}$)
R = 0.5 (RD7)	123	0.052	0.297	0.100	0.197
R = 4 (RD2)	168	0.071	0.358	0.149	0.209
R = 16 (RD8)	119	0.050	0.306	0.134	0.172

Fixed parameters: 6 h; 20 °C; pH = 3.

metry of the reaction depends on the experimental conditions and is satisfied for $R \in [3; 4]$. It was decided to consider the stoichiometric ratio of TMS as R = 4. Three syntheses were therefore carried out: one at R = 0.5, one at R = 4 and a final one at R = 16. The textural properties are given in Table 5 and the mesopore and micropore size distributions in Fig. 6A.

All the capsules were well dispersed after 6 h of reaction and none of the samples had flocculated or sedimented. The S_{BET}, V_{micro} and V_{meso} at R = 4 were slightly higher than at R = 0.5 and R = 16, for which the textural properties are more or less identical (Table 5). The micropore size distributions (Fig. 6A) show the same trend as V_{micro}: the distribution at R = 4 is higher than the other two across the entire micropore domain. The distributions at R = 0.5 and R = 16 nearly overlap over the entire micropore range. However, there is some difference between the mesopore size distributions of the different samples, particularly between 2 and 12 nm, where the three curves intersect (Fig. 6A). At R = 0.5, the curve increases progressively toward larger mesopores and there is no distinct peak except around 30 nm. At R = 4, the curve lies above that at R = 0.5 from 2 to 12 nm and forms a coarse peak centred at 5 nm. At R = 16, the curve is also above that at R = 0.5 from 2 to 12 nm and it also forms a coarse peak, this time centred at 9 nm. The ratio R mainly influences the kinetics of the hydrolysis reaction. When $R \ll 4$, hydrolysis is incomplete: many Si–OR bonds remain and only a few Si–OH bonds are available for condensation.[34,35,39,78,79] This leads to linear or weakly branched siloxane chains with many organic terminal groups and few silanols, which ultimately form an open fractal network composed of weakly connected linear primary particles.[34,35,39,78,79] When the water content leads to a stoichiometric ratio ($R \approx 4$), hydrolysis is largely completed: the formed gel remains a polymeric gel with an open fractal struc-

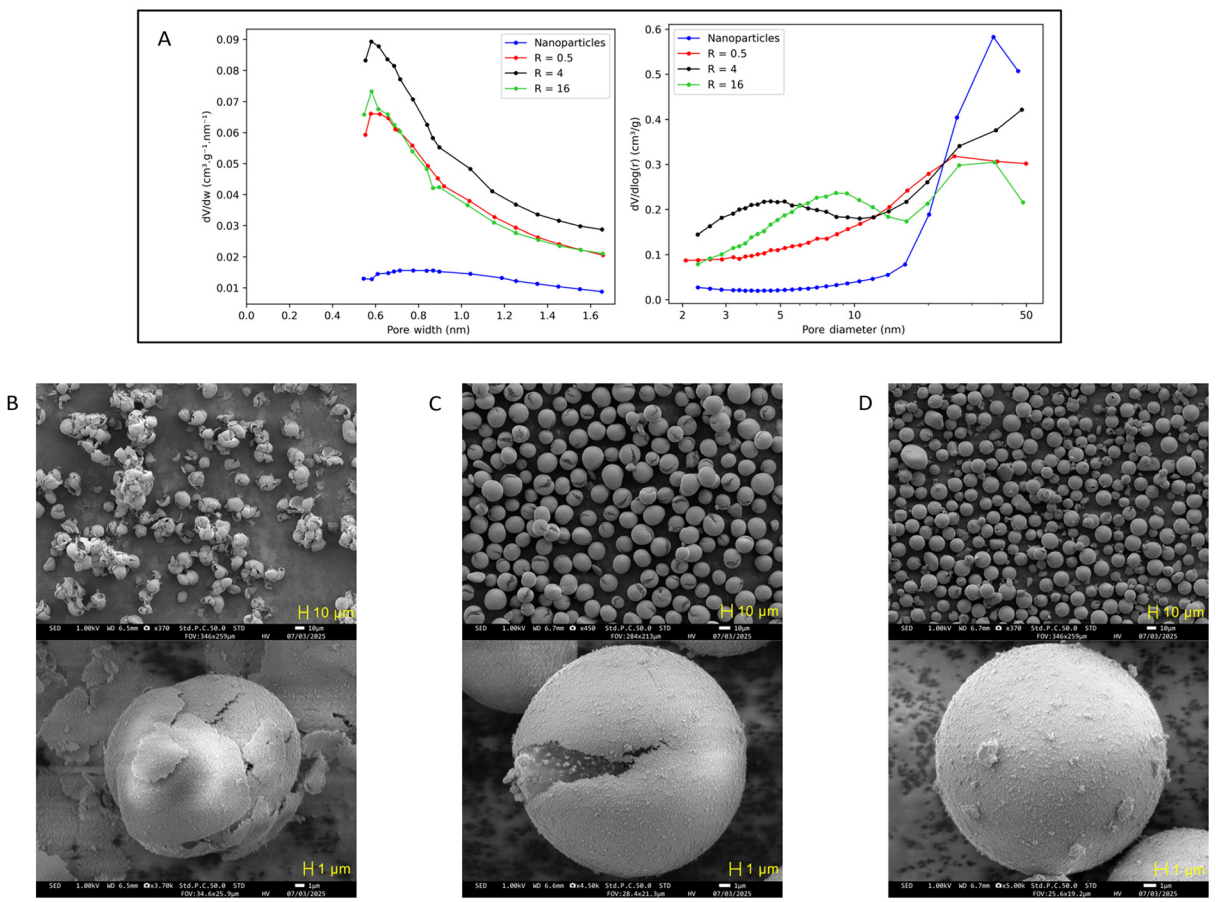

Fig. 6 (A) Size distributions of micropores and mesopores of capsules synthesized at different R ratios compared to the distributions of the nanoparticles used to make the Pickering emulsion. (B) SEM images of capsules synthesized at R = 0.5. (C) SEM images of capsules synthesized at R = 4. (D) SEM images of capsules synthesized at R = 16.

ture, but the network is much more cross-linked.[34,35,39,78,79] When there is a large excess of water ($R \gg 4$), hydrolysis is mostly complete and the relative rates of hydrolysis and condensation change: this produces many terminal Si–OH groups, and the hydrolysed monomers and short oligomers condense more slowly, which allows the formation of highly cross-linked particulate silica networks.[34,35,39,78,79]

The three syntheses carried out here were performed at a relatively acidic pH. At R = 0.5, the network is very open and includes micropores, mesopores and also macropores. As R increases, the network densifies and the large mesopores and macropores are replaced by smaller and smaller mesopores, which explains the coarse peak at 5 nm at R = 4. At R = 16, the increase in the average mesopore size could indicate that the silica gel structure has begun to transition from a fractal network to a particulate network.

As in previous studies, the capsules were analyzed by SEM (Fig. 6B–D). The capsules at R = 0.5 did not retain their structural integrity and broke into large fragments agglomerated together. At R = 16, the capsules not only retained their structural integrity and shape but were also barely ruptured or damaged, unlike all the other samples previously analyzed. As previously mentioned, at acidic pH and when R is low (R = 0.5), the network is primarily composed of weakly interconnected linear primary particles and oligomers forming an open, weakly cohesive fractal network; the capsules tend to break, even when dried with sCO_2, because the shell cannot support its own weight. At R = 4, hydrolysis is nearly complete; the network is more crosslinked and thus more cohesive, so the capsules retain some structural integrity compared to R = 0.5, but they are still almost all ruptured. Finally, at R = 16, hydrolysis is complete, and the resulting network is likely a hybrid between a highly crosslinked polymeric network and a colloidal network, forming capsules that retain their sphericity after supercritical CO_2 drying and do not break or rupture.

4. Conclusions

The influence of various synthesis and post-treatment parameters on the textural properties of silica capsules was systematically investigated. Drying with supercritical CO_2 was found to be essential for preserving the open structure of the silica shell and avoiding the collapse. Capsules dried with supercritical CO_2 retain high porosity and a relatively intact spherical shape, unlike those dried at room temperature and pressure, which exhibit cracks and significant shrinkage. Therefore, this drying step is a prerequisite for studying the effect of synthesis parameters on the intrinsic microstructure of the capsules.

All the studies carried out show that the porosity of silica capsules results from a trade-off between reaction kinetics and network cohesion. Theoretical optimal conditions for obtaining highly porous and mechanically stable capsules include gelation at moderate temperature (around 20 °C) for a limited time (6 hours), a strongly acidic environment (pH ≈ 0–1), and a high water-to-alkoxysilane R ratio. Future work combining these specific parameters will be needed to experimentally confirm this extrapolated optimum. These conclusions provide guidance for tailoring the capsules' microstructure according to the intended application. For example, highly microporous capsules would be sought for encapsulating small molecules, while mesoporous capsules are better suited for the controlled release of larger substances. Moreover, the work conducted in this study remains primarily structural. It would be worthwhile to evaluate how textural modifications influence capsule performance in application contexts (catalysis, encapsulation, and vectorization). Studies on the mechanical or thermal resistance of the capsules could also complement these findings, as well as exploration of alternative drying methods or new organosilicon precursors. Furthermore, future morphological characterization studies of these ultra-thin shells using SEM would greatly benefit from metallic sputtering (*e.g.*, gold coating) to prevent electron beam penetration and accurately resolve the shell thickness. Finally, the integration of specific chemical functionalities at the surface or within the capsule walls, *via* co-condensation of functionalized alkoxysilanes, could open the door to multifunctional hybrid materials.

Author contributions

Rémi Duclos: conceptualization, formal analysis, investigation, methodology, software, validation, visualization, writing – original draft, writing – review & editing, and visualization. Dina Lofficial: conceptualization, methodology, project administration, supervision, validation, and writing – review & editing. David Proriol: conceptualization, methodology, project administration, supervision, validation, and writing – review & editing. Christine Dalmazzone: conceptualization, methodology, project administration, supervision, validation, and writing – review & editing. Stéphane Parola: conceptualization and methodology. Frédéric Lerouge: conceptualization, methodology, project administration, supervision, validation, and writing – review & editing.

Conflicts of interest

There are no conflicts to declare.

Data availability

The data supporting this article have been included as part of the supplementary information (SI). Supplementary information is available. See DOI: https://doi.org/10.1039/d5nr05237h.

Acknowledgements

This work was carried out within the ECOCHEM project ANR-22-PESP-0006, funded by the PEPR Spleen Research Program, as part of the France 2030 investment plan.

References

1 Y. Zhang, B. Y. W. Hsu, C. Ren, X. Li and J. Wang, *Chem. Soc. Rev.*, 2015, **44**, 315–335.
2 X. Ma, H. Sui, Q. Yu, J. Cui and J. Hao, *Langmuir*, 2021, **37**, 3166–3172.
3 A. C. Jackson, J. A. Bartelt, K. Marczewski, N. R. Sottos and P. V. Braun, *Macromol. Rapid Commun.*, 2011, **32**, 82–87.
4 A. Shkatulov, R. Joosten, H. Fischer and H. Huinink, *ACS Appl. Energy Mater.*, 2020, **3**, 6860–6869.
5 R. Ciriminna, M. Sciortino, G. Alonzo, A. D. Schrijver and M. Pagliaro, *Chem. Rev.*, 2011, **111**, 765–789.
6 G. Cai, M. Ding, Q. Wu and H.-L. Jiang, *Natl. Sci. Rev.*, 2020, **7**, 37–45.
7 X. Zhang, Y. Hou, R. Ettelaie, R. Guan, M. Zhang, Y. Zhang and H. Yang, *J. Am. Chem. Soc.*, 2019, **141**, 5220–5230.
8 F. Joó, *Acc. Chem. Res.*, 2002, **35**, 738–745.
9 N. Thi Kim Chau, S. Kim, H.-J. Lee, M. Lee and Y.-M. Chung, *Chem. Commun.*, 2024, **60**, 168–171.
10 C. W. Kohlpaintner, R. W. Fischer and B. Cornils, *Appl. Catal., A*, 2001, **221**, 219–225.
11 M. Haumann and A. Riisager, *Chem. Rev.*, 2008, **108**, 1474–1497.
12 V. I. Pârvulescu and C. Hardacre, *Chem. Rev.*, 2007, **107**, 2615–2665.
13 L. Magna, J. Bildé, H. Olivier-Bourbigou, T. Robert and B. Gilbert, *Oil Gas Sci. Technol.*, 2009, **64**, 669–679.
14 L. K. S. Gujjala, D. Kundu, D. Dutta, A. Kumar, M. Bal, A. Kumar, E. Singh, R. Mishra, S. Kumar and D.-V. N. Vo, *J. Mol. Liq.*, 2024, **396**, 123896.
15 S. Zhang, Y. Huang, L. Zhang, Y. Liu, Q. Miao, R. Liu, W. Zhao, Y. Diao and K. Dong, *Green Chem.*, 2024, **26**, 9048–9074.
16 K. Dutkowski, M. Kruzel, M. Smuga-Kogut and M. Walczak, *Energies*, 2025, **18**, 4053.
17 M. Zhang, R. Ettelaie, T. Yan, S. Zhang, F. Cheng, B. P. Binks and H. Yang, *J. Am. Chem. Soc.*, 2017, **139**, 17387–17396.
18 S. Zhang, J. Zhang, Y. Zhang and Y. Deng, *Chem. Rev.*, 2017, **117**, 6755–6833.
19 J. Yan and F. Mangolini, *RSC Adv.*, 2021, **11**, 36273–36288.
20 Y. Chevalier and M.-A. Bolzinger, *Colloids Surf., A*, 2013, **439**, 23–34.
21 H. Jiang, Y. Sheng and T. Ngai, *Curr. Opin. Colloid Interface Sci.*, 2020, **49**, 1–15.
22 Q. Luo, Y. Wang, Z. Chen, P. Wei, E. Yoo and E. Pentzer, *ACS Appl. Mater. Interfaces*, 2019, **11**, 9612–9620.
23 L. Wei, S. Yan, H. Wang and H. Yang, *NPG Asia Mater.*, 2018, **10**, 899–911.
24 S. A. F. Bon and T. Chen, *Langmuir*, 2007, **23**, 9527–9530.
25 A. Ganguly, T. Ahmad and A. K. Ganguli, *Langmuir*, 2010, **26**, 14901–14908.
26 S. Che, H. Li, S. Lim, Y. Sakamoto, O. Terasaki and T. Tatsumi, *Chem. Mater.*, 2005, **17**, 4103–4113.
27 C. Gao, H. Qiu, W. Zeng, Y. Sakamoto, O. Terasaki, K. Sakamoto, Q. Chen and S. Che, *Chem. Mater.*, 2006, **18**, 3904–3914.
28 D. Kuang, T. Brezesinski and B. Smarsly, *J. Am. Chem. Soc.*, 2004, **126**, 10534–10535.
29 M. Graham and D. Shchukin, *Langmuir*, 2021, **37**, 918–927.
30 C. J. Brinker, *J. Non-Cryst. Solids*, 1988, **100**, 31–50.
31 M. D. Curran and A. E. Stiegman, *J. Non-Cryst. Solids*, 1999, **249**, 62–68.
32 M.-J. Muñoz-Aguado and M. Gregorkiewitz, *J. Colloid Interface Sci.*, 1997, **185**, 459–465.
33 Ö. Kesmez, E. Burunkaya, N. Kiraz, H. E. Çamurlu, M. Asiltürk and E. Arpaç, *J. Non-Cryst. Solids*, 2011, **357**, 3130–3135.
34 I. Strawbridge, A. F. Craievich and P. F. James, *J. Non-Cryst. Solids*, 1985, **72**, 139–157.
35 X. Zhao, Y. Wang, J. Luo, P. Wang, P. Xiao and B. Jiang, *Silicon*, 2021, **13**, 3413–3421.
36 K. Müller, C. Scherdel, S. Vidi, G. Reichenauer, M. Boxheimer, F. Dehn and D. Enke, *Gels*, 2025, **11**, 196.
37 L. Zhang, M. D'Acunzi, M. Kappl, A. Imhof, A. V. Blaaderen, H.-J. Butt, R. Graf and D. Vollmer, *Phys. Chem. Chem. Phys.*, 2010, **12**, 15392.
38 J. Estella, J. C. Echeverría, M. Laguna and J. J. Garrido, *Microporous Mesoporous Mater.*, 2007, **102**, 274–282.
39 C. A. Milea, C. Bogatu and A. Duta, *Bulletin of the Transilvania University of Braşov, Series I: Engineering Sciences*, 2011, **4**, 53.
40 M. Thommes, K. Kaneko, A. V. Neimark, J. P. Olivier, F. Rodriguez-Reinoso, J. Rouquerol and K. S. W. Sing, *Pure Appl. Chem.*, 2015, **87**, 1051–1069.
41 K. S. W. Sing, *Pure Appl. Chem.*, 1985, **57**, 603–619.
42 X. Cui, S. Zhang, F. Shi, Q. Zhang, X. Ma, L. Lu and Y. Deng, *ChemSusChem*, 2010, **3**, 1043–1047.
43 C. Thomazeau, H. Olivier-Bourbigou, L. Magna, S. Luts and B. Gilbert, *J. Am. Chem. Soc.*, 2003, **125**, 5264–5265.
44 C. J. Brinker and G. W. Scherer, *Sol-gel science: the physics and chemistry of sol-gel processing*, Academic Press, 1990.
45 D. M. Smith, G. W. Scherer and J. M. Anderson, *J. Non-Cryst. Solids*, 1995, **188**, 191–206.
46 M. Roozbahani, R. Borela and J. Frost, *Materials*, 2017, **10**, 1237.
47 J. Gonthier, E. Scoppola, T. Rilling, A. Gurlo, P. Fratzl and W. Wagermaier, *Langmuir*, 2024, **40**, 12925–12938.
48 T. Fernique, *Exp. Math.*, 2024, **33**, 235–246.
49 T. Kawaguchi, H. Hishikura and J. Iura, *J. Non-Cryst. Solids*, 1988, **100**, 220–225.
50 G. W. Scherer, *J. Non-Cryst. Solids*, 1997, **215**, 155–168.
51 J. Sakamoto, R. P. Maloney and T. Thompson, Porous sol gels and methods and structures related thereto, US9808964B2, 2017.
52 C. A. García-González, M. C. Camino-Rey, M. Alnaief, C. Zetzl and I. Smirnova, *J. Supercrit. Fluids*, 2012, **66**, 297–306.
53 U. Ali, R. Meinusch, K. Turke, P. R. Schreiner and B. M. Smarsly, *Langmuir*, 2025, **41**, 13845–13859.

54 R. Meinusch, R. Ellinghaus, K. Hormann, U. Tallarek and B. M. Smarsly, *Phys. Chem. Chem. Phys.*, 2017, **19**, 14821–14834.
55 A. Galarneau, H. Cambon, F. Di Renzo, R. Ryoo, M. Choi and F. Fajula, *New J. Chem.*, 2003, **27**, 73–79.
56 F. E. D. Silva, E. Rigoti, M. I. S. D. Mello and S. B. C. Pergher, *Materials*, 2024, **17**, 2827.
57 T. Benamor, L. Vidal, B. Lebeau and C. Marichal, *Microporous Mesoporous Mater.*, 2012, **153**, 100–114.
58 K. Nakanishi, *J. Porous Mater.*, 1997, **4**, 67–112.
59 R. F. Silva and W. L. Vasconcelos, *Mater. Res.*, 1999, **2**, 197–200.
60 L. Zhang, M. D'Acunzi, M. Kappl, G. K. Auernhammer, D. Vollmer, C. M. van Kats and A. van Blaaderen, *Langmuir*, 2009, **25**, 2711–2717.
61 P. J. Davis, C. J. Brinker and D. M. Smith, *J. Non-Cryst. Solids*, 1992, **142**, 189–196.
62 S. V. Homburg and A. V. Patel, *Polymers*, 2022, **14**, 1391.
63 M. Zielecka, E. Bujnowska, K. Suwala and M. Wenda, *Recent Applications in Sol-Gel Synthesis*, InTech, 2017.
64 R. Gutiérrez-Climente, M. Clavié, P. Dumy, A. Mehdi and G. Subra, *J. Mater. Chem. B*, 2021, **9**, 2155–2178.
65 C. J. Brinker and G. W. Scherer, *J. Non-Cryst. Solids*, 1985, **70**, 301–322.
66 D. J. Belton, O. Deschaume and C. C. Perry, *FEBS J.*, 2012, **279**, 1710–1720.
67 Z. V. Faustova and Y. G. Slizhov, *Inorg. Mater.*, 2017, **53**, 287–291.
68 F. Salaün, C. Butstraen and E. Devaux, *Science and Technology Behind Nanoemulsions*, InTech, 2018.
69 C. R. Silva and C. Airoldi, *J. Colloid Interface Sci.*, 1997, **195**, 381–387.
70 E. Keleş Güner and A. Özer, *Sigma J. Eng. Nat. Sci.*, 2019, **37**, 1195–1202.
71 J. C. Ro and J. C. In, *J. Non-Cryst. Solids*, 1991, **130**, 8–17.
72 B. L. Cushing, V. L. Kolesnichenko and C. J. O'Connor, *Chem. Rev.*, 2004, **104**, 3893–3946.
73 C. J. Brinker, W. D. Drotning and G. W. Scherer, *MRS Online Proc. Libr.*, 1984, **32**, 25.
74 A. Erigoni and U. Diaz, *Catalysts*, 2021, **11**, 79.
75 D. A. Schneider, B. M. Baugher, D. A. Loy, K. Rahimian and T. Alam, *MRS Online Proc. Libr.*, 2000, **628**, 635.
76 R. E. Kirk, D. F. Othmer, J. I. Kroschwitz and M. Howe-Grant, *Encyclopedia of chemical technology*, J. Wiley & sons, 1997.
77 M. Pauthe, J. Phalippou, R. Corriu, D. Leclercq and A. Vioux, *J. Non-Cryst. Solids*, 1989, **113**, 21–30.
78 B. Xia, L. Yan, Y. Li, S. Zhang, M. He, H. Li, H. Yan and B. Jiang, *RSC Adv.*, 2018, **8**, 6091–6098.
79 D. L. Meixner and P. N. Dyer, *J. Sol-Gel Sci. Technol.*, 1999, **14**, 223–232.
80 V. Baranau and U. Tallarek, *Soft Matter*, 2014, **10**, 3826.